Sharp tuning of head direction by somatosensory fast-spiking interneurons

Xiaoyang Long[1], Calvin K. Young[2] and Sheng-Jia Zhang[1,*]

1Department of Neurosurgery, Xinqiao Hospital, Army Medical University, Chongqing, China

2Department of Psychology, Brain Health Research Centre, University of Otago, Dunedin, New Zealand

*To whom correspondence should be addressed.

Correspondence and requests for materials should be addressed to: sheng-jia.zhang@tmmu.edu.cn or sheng-jia.zhang@outlook.com

Abstract

Head direction (HD) information is intricately linked to spatial navigation and cognition. We recently reported the co-existence of all currently recognized spatial cell types can be found in the hindlimb primary somatosensory cortex (S1HL). In this study, we carried out an in-depth characterization of HD cells in S1HL. We show fast-spiking (FS), putative inhibitory neurons are over-represented in and sharply tuned to HD compared to regular-spiking (RS), putative excitatory neurons. These FS HD cells are non-conjunctive, rarely theta modulated, not locally connected and are enriched in layer 4/5a. Their co-existence with RS HD cells and angular head velocity (AHV) cells in a layer-specific fashion through the S1HL presents a previously unreported organization of spatial circuits. These findings challenge the notion that FS, putative inhibitory interneurons are weakly tuned to external stimuli in general and present a novel local network configuration not reported in other parts of the brain.

Key Words: head direction cell, fast-spiking neuron, somatosensory cortex, spatial navigation system, angular head velocity cell, theta modulation

Introduction

The ability to navigate from one place to another requires the knowledge of self in space. While hippocampal-entorhinal systems appear to map out the spatial environment (Hafting et al., 2005; O'Keefe and Dostrovsky, 1971; Solstad et al., 2008), the head direction (HD) system maintains an internally generated reference point to anchor our orientation in space. Cells that are tuned to HD were first reported in the rat postsubiculum (Taube et al., 1990a), which are strongly modulated by salient visual cues (Taube et al., 1990a, b). The neural substrate of HD cell activity has been shown to be dependent on vestibular input (Stackman et al., 2002; Stackman and Taube, 1997). The existence of cells responsive to the speed of angular head displacement (angular head velocity; AHV cells) and connection patterns between the lateral mammillary nucleus and the dorsal tegmental nucleus prompted the suggestion that a ring attractor network involving these structures may generate and propagate the HD signal throughout the brain (Clark and Taube, 2012).

The importance of the HD system in the spatial representation of the brain is highlighted by the persistence of HD representation upon manipulations that abolish position representation in hippocampal place cells (Bolding et al., 2019) and entorhinal grid cells (Brandon et al., 2011; Koenig et al., 2011). Particularly HD representations survive in cells that code HD conjunctively with grid or border representations (Brandon et al., 2011). Conversely, the elimination of HD signal into parahippocampal cortices through anteriodorsal thalamic nucleus lesions significantly disrupts HD, place (Calton et al., 2003; Harland et al., 2017; Stackman et al., 2002) and grid (Winter et al., 2015) cell signals. Therefore, available evidence suggests HD signaling goes beyond egocentric spatial representation and is also crucial for maintaining allocentric spatial representation.

It is known that if animals are deprived of sensorimotor input through passive transport by a cart, HD cells cannot maintain stable tuning (Stackman et al., 2003). If rotated passively, HD tuning may be intact but with greatly reduced firing rates (Knierim et al., 1998; Taube, 1995; Taube et al., 1990b) attributable to a mismatch of sensorimotor signals from insufficient head restraint (Shinder and Taube, 2011), suggesting self-motion is crucial for normal HD representation (Shinder and Taube, 2014). Similar properties exist for AHV cells, where passive rotation abolishes AHV in a subset of cells (Sharp et al., 2001). Collectively, these data point to the importance of sensorimotor input in the maintenance and persistence of HD activity.

Spatial selectivity in the brain has long been assumed to be the properties of specialized regions centered around the temporal cortex. More recent investigations suggest spatial representation may be more widespread than previously thought (Hok et al., 2018; Jankowski and O'Mara, 2015; Long and Zhang, 2018). We have recently discovered all currently recognized spatial cell types can be found in the rat hindlimb region of the primary somatosensory cortex (S1HL), including HD cells (Long and Zhang, 2018). In the current study, we carried out an in-depth characterization of S1HL HD and AHV cells. Remarkably, HD representation is not exclusive to regular-spiking (RS) putative principal cells. In fact, fast-spiking (FS) putative interneurons predominate HD representation with sharper tuning and appear to be enriched in layer 4/5a of S1HL and are not locally connected. AHV was also better tuned in FS and outnumber their RS counterparts, demonstrating a split layer distribution non-overlapping with FS HD cells. Our findings challenge the prevailing view that inhibitory interneurons are only broadly tuned to input stimuli and present a novel network configuration of, and a function for, HD representation in the brain.

Results

Somatosensory regular-spiking and fast-spiking HD cells

Putative single-cell recordings (**Supplementary Fig. S1**) through the S1HL (**Fig. 1a**) were obtained from seven rats performing a pellet chasing task in an open field (1 m x 1 m). As described previously (Long and Zhang, 2018), HD tuned cells can be found in the S1HL (**Fig. 1b**). The HD selectivity is stable within sessions (**Supplementary Fig. S2**) and is not biased by location (**Supplementary Fig. S3**). Neurons with mean vector length exceeding the 99th percentile of the population distribution were classified as HD cells (**Fig. 1c**). To examine the relative contribution of putative excitatory and inhibitory neurons, we classified recorded neurons based on their spike widths and firing rates (**Fig. 1d**). From these criteria, we report 120/2107 (5.7%) cells being HD cells. Among HD cells, 62/120 (52%) were classified as regular-spiking (RS), 36/120 (30%) were classified as fast-spiking (FS) and 22/120 (18%) were unclassified (**Supplementary Fig. S4**). Only 44% of the RS HD cells were "pure" HD cells with no detectable conjunctive representation while 100% of the FS HD cells coded for HD exclusively (**Supplementary Fig. S4**). We did not find a difference in how well conjunctive and non-conjunctive cells coded for HD (**Supplementary Fig. S5**); hence

92 we included all classified HD cells (i.e. conjunctive and non-conjunctive) for
93 subsequent analyses. Both populations showed uniform distribution of HD tuning (χ^2-
94 test; P = 0.82 for FS HD cells and P = 0.81 for RS HD cells; **Fig. 1e**) From
95 reconstructed tetrode tracks, the spatial distribution of RS and unclassified HD cells
96 appear to be uniformly distributed across layers 3 to 6, while FS HD cells are enriched
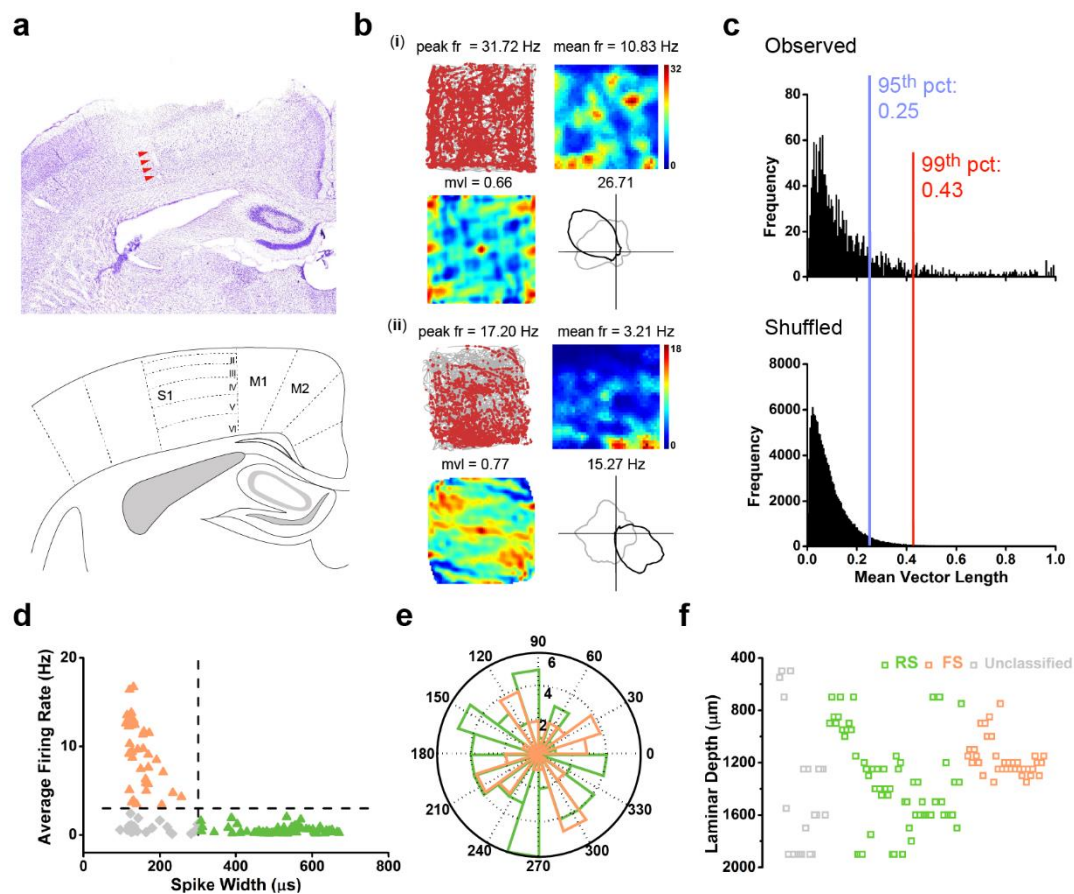97 between layer 4 and 5a, avoiding deeper layers altogether (**Fig. 1f**).

98

99 **Fig. 1: Both regular-spiking (RS) and fast-spiking (FS) cells are tuned to head**
100 **direction in the S1HL**

101 **a,** A representative Nissl-stained coronal section shows tetrode trajectory (indicated
102 with red arrowheads) tracking through all of six layers across the rat primary
103 somatosensory cortex (top). Idealized S1 layer boundaries are depicted on the
104 reference atlas (bottom). **b**, Two representative somatosensory HD cells. Trajectory
105 (grey line) with superimposed spike locations (red dots; top left), smoothed rate maps
106 (top right), spatial autocorrelation (bottom left) and HD tuning curves (black) plotted
107 against dwell-time (grey) in polar coordinates (bottom right). Firing rate is color-coded
108 with dark blue indicating minimal firing rate and dark red indicating maximal firing rate.

109   The scale of the autocorrelation maps is twice that of the spatial firing rate maps. Peak

110   firing rate (fr), mean fr, mean vector length (mvl) and angular peak rate for each

111   representative HD cell are labeled at the top of the plots. **c**, Distribution of mean vector

112   length for the entire pool of recorded somatosensory cells. The top panel shows the

113   distribution for observed values. The bottom panel shows the distribution for randomly

114   shuffled data from the same pool of recorded S1HL. **d**, Distribution of the average

115   firing rate versus peak-to-through distance (spike widths) shows three classes of HD

116   cells: regular-spiking (RS; green), fast-spiking (FS; orange) and the unclassified cells

117   (gray). **e**, The circular distribution of the preferred direction for two discrete FS (orange)

118   and RS (green) groups from all seven animals. **f**, Reconstructed recording depth for

119   all S1HL HD cells.

Sharply tuned fast-spiking HD cells

121   FS tuning to HD has been described as being weak within the canonical HD circuit

122   (Peyrache et al., 2019; Tsanov et al., 2011; Tukker et al., 2015), and only a single

123   study to date has reported FS HD tuning comparable to RS HD cells in the

124   hippocampus (Leutgeb et al., 2000). Therefore, we sought to examine how HD tuning

125   varied between RS and FS. Remarkably, we found that RS HD cells were generally

126   less well-tuned (**Fig. 2a, c**) compared to FS HD cells (**Fig. 2b, d**). Given FS cells have

127   higher firing rates which could potentially inflate HD tuning measures, we

128   downsampled FS firing by randomly omitting spikes from the raw spike train to match

129   the average firing rate of RS HD cells (**Fig. 2f**) to test if the sharper FS HD tuning

130   persists (e.g. **Fig. 2e**). Downsampling did not change the mean vector length (**Fig. 2g**),

131   tuning width (**Fig. 2h**) and angular stability (**Fig. 2i**) of FS HD cells and all these

132   measures remained significantly higher than RS HD cells (**Fig. 2g-i**). These data

133   collectively showed FS HD cells are better tuned than their RS counterparts,
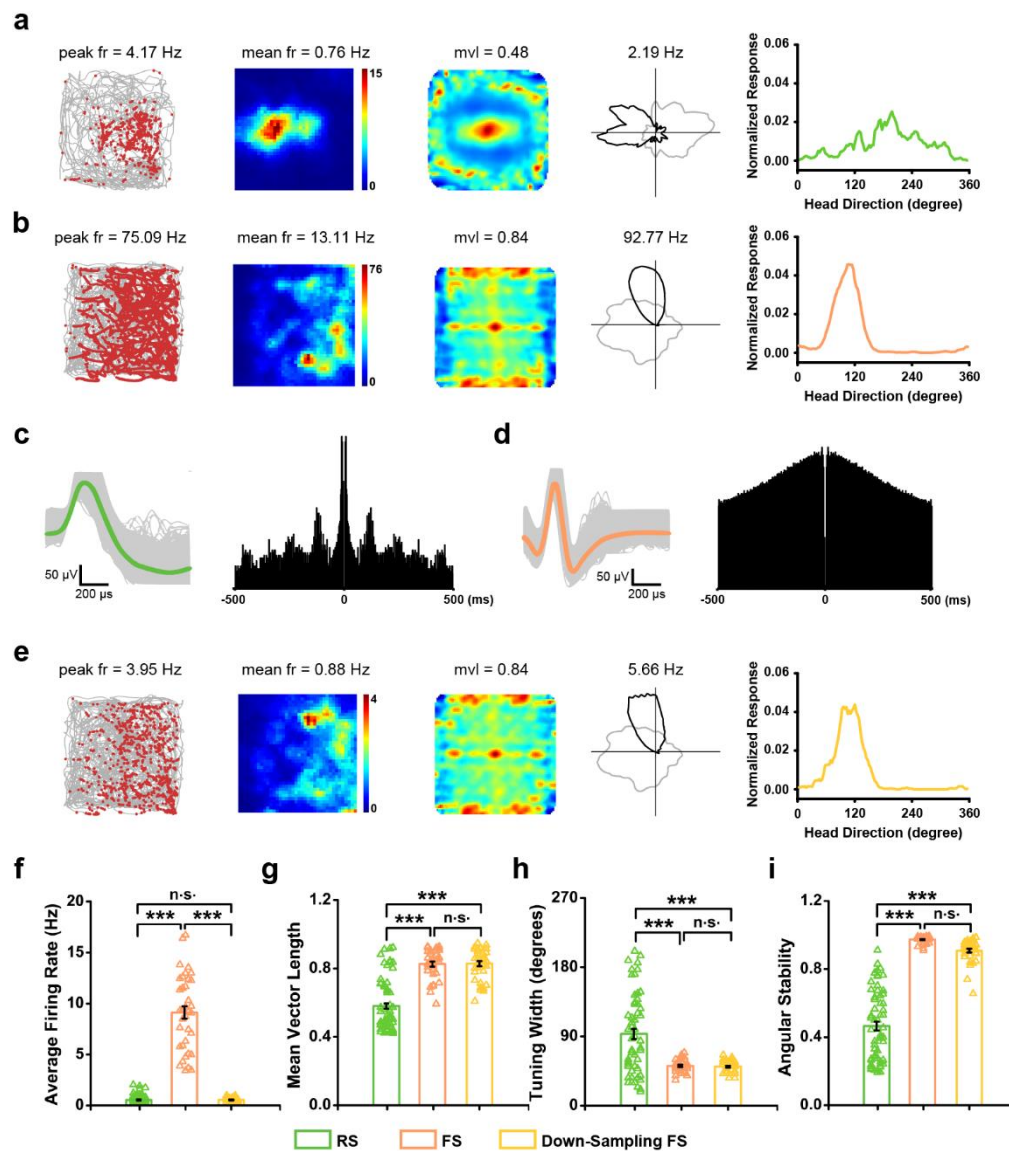
134   independent of spike number.

Fig. 2: Sharper tuning of fast-spiking head direction cells.

a, b, Two representative examples of somatosensory RS (**a**) and FS (**b**) HD cells. From left to right, trajectory (grey line) with superimposed spike locations (red dots) (left), smoothed rate maps, spatial autocorrelation, HD tuning curves (black) plotted against dwell-time and tuning curves are presented. Firing rate is color-coded with dark blue indicating minimal firing rate and dark red indicating maximal firing rate. The scale of the autocorrelation maps is twice that of the spatial firing rate maps. Peak firing rate (fr), mean fr, mean vector length (mvl) and angular peak rate for each representative head direction cell are labelled at the top of the panels. **c, d,** waveform of the representative RS HD cell (left in **c**) displays the longer spike duration than that of the representative FS HD cell (left in **d**). Representative 1000 ms spike-time autocorrelogram of the RS HD cell (right in **c**) shows a faster decay than that of the

148   FS HD cell (right in **d**). **e**. Downsampled data for the FS HD cell depicted in (**b**). **f**,

149   Comparable average firing rates between RS HD cells and downsampled FS HD cells.

150   **g**, Mean vector lengths of FS HD cells (orange, $n = 36$) as well as downsampled FS

151   HD cells (yellow, $n = 36$) are significantly higher than that of RS HD cells (green, $n =$

152   62). Mean vector lengths of FS HD cells do not differ between full-sampled and

153   downsampled data. **h**, RS HD cells have wider tuning than FS HD cells and

154   downsampled FS HD cells. **i**, FS HD cells and downsampled FS HD cells show higher

155   angular stability than RS HD cells. Data are means ± s.e.m.; ***$P < 0.001$, two-tailed

156   unpaired *t*-test for RS HD vs FS HD cells or vs down-sampled FS HD cells; two-tailed

157   paired *t*-test for FS HD cells versus down-sampled FS HD cells (**f-i**). green, RS; orange,

158   FS; yellow, down-sampling FS.

Weakly theta-modulated FS HD cells

160   Theta oscillations in the limbic system have been implicated in the integration of spatial

161   inputs (Burgess and O'Keefe, 2011) and are necessary for the normal place (Bolding

162   et al., 2019) and grid (Brandon et al., 2011; Koenig et al., 2011) cell activities. However,

163   theta modulation of HD cells, in general, appears to be location- and cell type-

164   dependent (Blair et al., 1999; Leutgeb et al., 2000; Preston-Ferrer et al., 2016; Sharp,

165   1996; Tsanov et al., 2011; Tukker et al., 2015). Therefore, we sought to characterize

166   theta modulation of HD cells in the S1HL. Firstly, theta oscillations can be detected in

167   the S1HL (**Fig. 3a**). An example of theta modulated RS HD cell autocorrelogram was

168   shown in **Fig. 3c** and a non-theta modulated FS HD cell are shown in **Fig. 3d**. In

169   general, spectral distribution of autocorrelograms of RS HD cells revealed a large peak

170   at 7.5 Hz (**Fig. 3f**), while FS HD cell autocorrelograms had a nominal low frequency

171   (< 2 Hz) peak (**Fig. 3g**). Most of the HD cells, RS or FS, had low percentage power in

172   their spike autocorrelogram spectra (**Fig. 3e**). However, a subset of RS HD cells and

173   a very few FS HD cells exhibited higher percentage theta power and were deemed to

174   be theta modulated (**Fig. 3h**). In fact, there was a 15 fold difference in the proportion

175   of RS (41.9%) and FS (2.8%) HD cells that were found to be theta modulated (**Fig. 3i**).
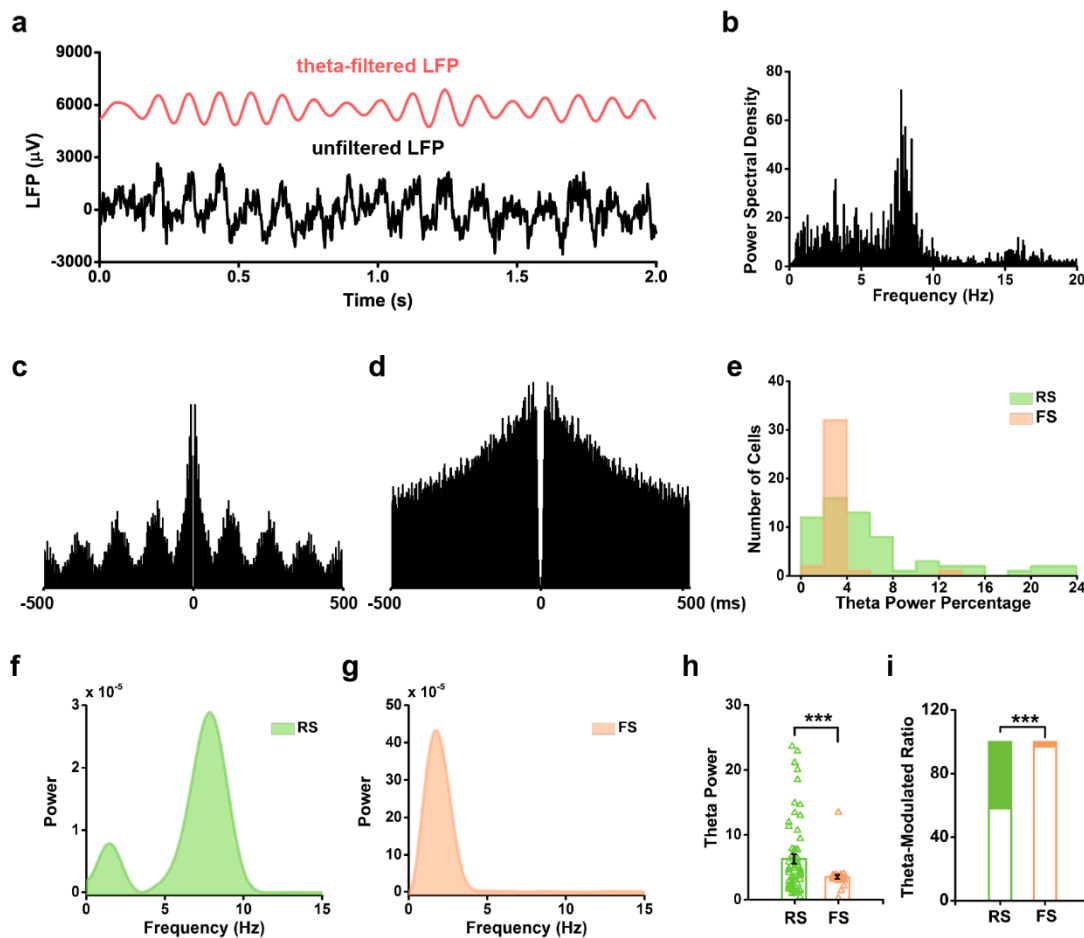
Fig. 3: Fast-spiking head direction cells show little theta modulation.

a, Prominent theta oscillations in the S1HL during locomotion. The unfiltered signal is in black and theta-filtered (4-11 Hz) signal is in red. **b**, Power spectral density for the whole recordings session shown in **a**. **c-d,** Two representative spike-time autocorrelograms of RS (**c**) and FS (**d**) HD cells. The RS HD cell shows clear theta modulation. **e**. Distribution of theta power percentage in the power spectrum of spike-time autocorrelograms of RS and FS HD cells. **f-g**. The power spectrum of spike-time autocorrelograms of the representative RS (**c**) and FS (**d**) HD cells, respectively. **h**. RS HD cells show significantly higher theta power percentage than FS HD cells. (mean ± s.e.m.; ***$P < 0.001$, two-tailed unpaired t-test). **i**. The fraction of theta-modulated RS HD cells (26/62) was significantly higher than that of FS HD cells (1/36) ($Z = -4.16$, ***$P < 0.001$, binomial test).

FS HD cells in bursty discharge patterns

Bursting activity has been shown to play pivotal functions in spatial selectivity and orientation (Ebbesen et al., 2016). We found that FS HD cells exhibited bursting

192 activity when the animals' heads oriented in their preferred direction (**Fig. 4a**). The

193 interspike intervals (ISI) histogram revealed the distinct temporal discharge patterns

194 for RS and FS HD cells (**Fig. 4d**). Consistent with previous studies (Ebbesen et al.,

195 2016; Latuske et al., 2015), the first two principal components of ISI distribution

196 probability distinguished RS and FS cells (**Fig. 4b**). The bursty firing pattern of FS HD

197 cells was also reflected in the cumulative probability distributions, with ISI being
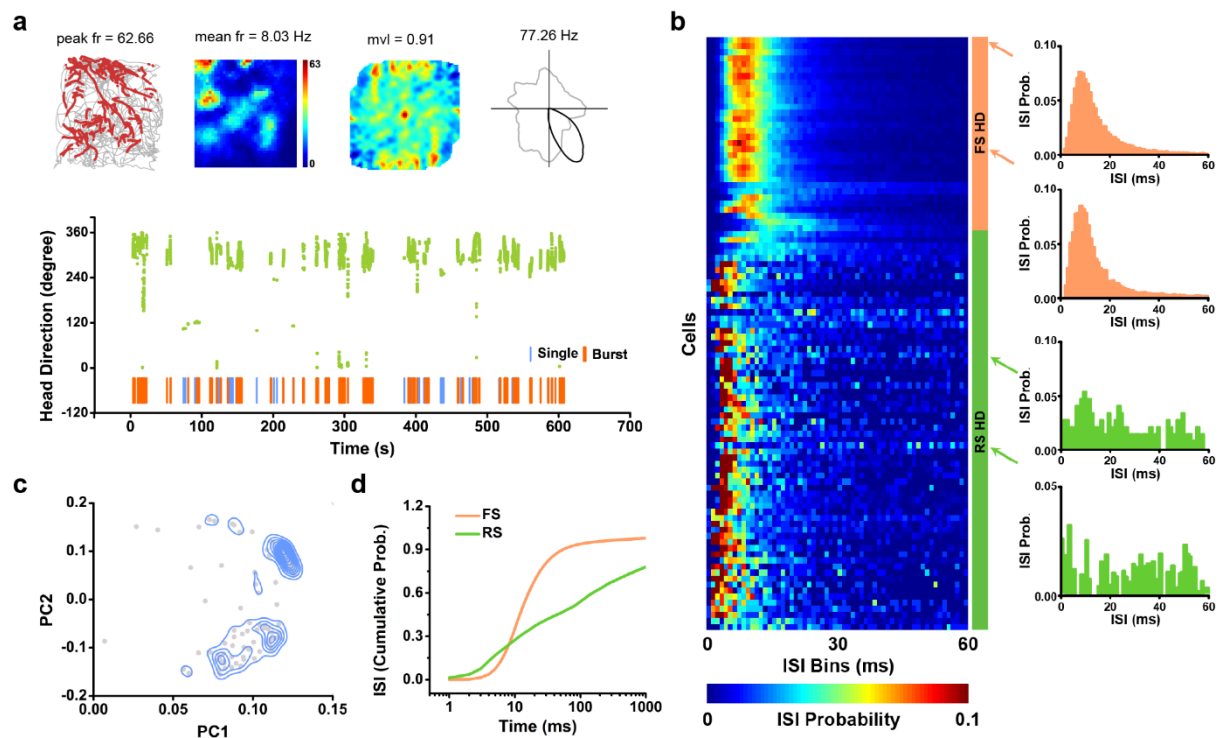
198 shorter than 20 ms (**Fig. 4c**).

199

Fig. 4: Fast-spiking head direction cells exhibit bursty firing mode.

201 **a**, A representative example of FS HD cell discharging in a bursty pattern. From left to

202 right, plots show: trajectory (grey line) with superimposed spike locations (red dots);

203 smoothed rate maps; spatial autocorrelation; and head direction tuning (black) against

204 dwell-time plot (grey). Firing rate is color-coded with dark blue indicating minimal firing

205 rate and dark red indicating maximal firing rate. The scale of the autocorrelation maps

206 is twice that of the spatial firing rate maps. Peak firing rate (fr), mean fr, mean vector

207 length (mvl) and angular peak rate for each representative HD cell are labeled at the

208 top of the panels. Below, the raster plot of the spike train emitted by the FS HD cell

209 and corresponding HD (green dots). FS HD cell fires trains of burst spikes when the

210 animal's HD matches the cell's preferred direction. Single spikes and bursty trains of

211 spikes emitted by the FS HD cells are discriminated by ISI of 15 ms. **b**, ISI histograms

212   (left) of pooled FS and RS HD cells, sorted by average firing rate. Representative ISI

213   histograms of two somatosensory FS HD cells (upper right, orange) and two RS HD

214   cells (lower right, green). FS HD cells tend to fire burst at 50-250 Hz (4- to 20-ms

215   intervals). **c**, A principal component analysis is computed based on the ISI distribution.

216   Scatterplot shows the first two principal components (PC1 and PC2 with 2D kernel

217   smoothed density estimate in blue lines). **d**, Cumulative probability distribution of

218   interspike intervals (ISI) for FS and RS HD cells. FS HD cells fired with ISI shorter than

219   20 ms.

Somatosensory angular head velocity cells

221   The generation of HD selectivity is believed to involve AHV cells in proposed ring

222   attractor models (Stratton et al., 2010; Zhang, 1996). A recent report showed that AHV

223   cells can be found alongside HD cells in the neighboring motor cortex (Mehlman et al.,

224   2019). Therefore, we hypothesized AHV cells should also be present in the S1HL. A

225   total of 308/2107 putative single units recorded from the S1HL were classified as AHV

226   cells (e.g. **Fig 5a**, **b**). Both symmetrical and asymmetrical AHV cells were found in the

227   S1HL (**Fig. 5c**, **d**). As with HD cells, we further extended our AHV cell characterization

228   with RS and FS AHV classification (**Fig. 5e**). Most AHV cells were non-conjunctive,

229   and the most common conjunctive feature was HD (**Supplementary Fig. S6**), followed

230   by location selectivity (i.e. exhibiting place cell-like selectivity; **Supplementary Fig.**

231   **S7**). Almost half of the AHV cells were FS cells, which also had statistically significant

232   higher AHV scores than RS AHV cells as a group (**Fig. 5f**). A large majority (85.7%)

233   of RS AHV cells and a half (50%) of the FS AHV cells were found to be theta modulated

234   (**Fig. 5h, j**); there appeared to be clear segregation of non-modulated and modulated

235   cells based on our classification (**Fig. 5i**). Of note, a much larger proportion of FS AHV

236   cells were found to be theta modulated than FS HD cells (**Fig. 5j**). Unlike the pattern

237   seen for HD cells, RS AHV cells appear to dominate layers 3 while FS AHV cells were

238   more common in layer 5 and deeper; layer 4 seemed to contain the least number of

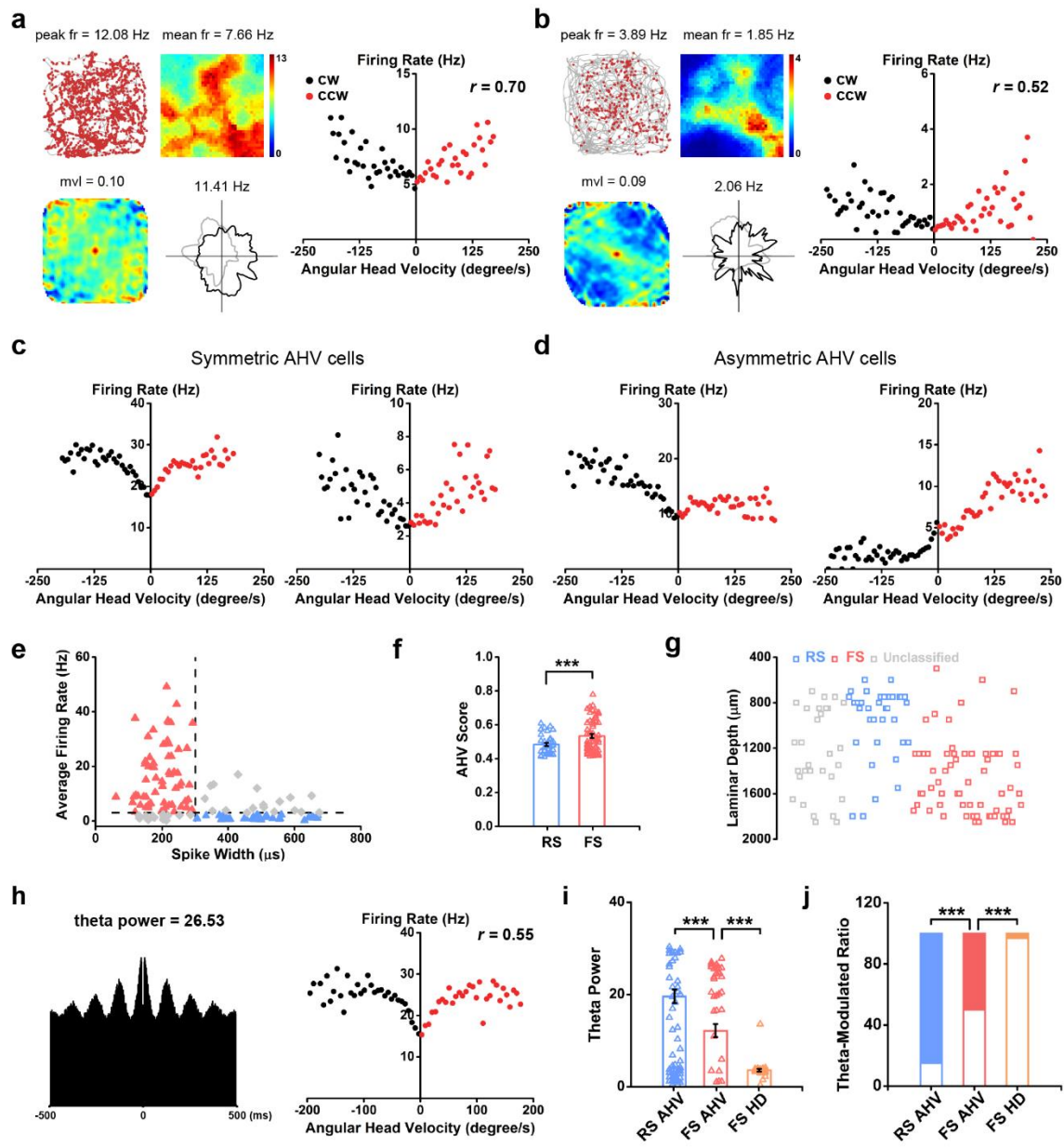239   AHV cells (**Fig. 5g**).

240

241

Fig. 5: Somatosensory regular-spiking (RS) and fast-spiking (FS) angular head velocity cells.

a, A representative FS AHV cell. Trajectory (grey line) with superimposed spike locations (red dots) (top left), smoothed rate maps (top right), spatial autocorrelation bottom left and HD tuning curves (black) plotted against dwell-time (grey; bottom right). Firing rate is color-coded with dark blue indicating minimal firing rate and dark red indicating maximal firing rate. The scale of the autocorrelation maps is twice that of the spatial firing rate maps. Peak firing rate (fr), mean firing fr, mean vector length (mvl) and angular peak rate for each representative head direction cell are labelled at the top of the panels. Right, the scatterplot of binned firing rates versus angular head

252 velocity. **b**, The same as **a** but for a representative RS AHV cell. **c**, Two examples of

253 symmetric AHV cells. **d**, Two representative asymmetric AHV cells. **e**, Distribution of

254 the average firing rate vs peak-to-through distance (spike widths) defines three

255 classes of AHV cells: RS (blue), FS (red) and unclassified (gray). **f**, The averaged AHV

256 score of FS AHV cells is substantially higher than that those of RS AHV cells. Data

257 are means ± s.e.m.; ***$P < 0.001$, two-tailed unpaired t-test. **g**, The reconstructed

258 depth distribution of recorded AHV cells. **h**, Representative example of somatosensory

259 theta-modulated FS AHV cell. Left, the spike-time autocorrelogram; Right, the

260 scatterplot of the firing rate versus the angular velocity of the representative AHV cell.

261 Theta power and correlation coefficient (r) are labelled at the top of the panel. **i**, Theta

262 power of FS AHV cells (red) compared to RS AHV cells and FS HD cells. **j**, The ratio

263 of theta-modulated FS AHV cells (31/62, 50%) is significantly higher than that of FS

264 HD cells (1/36, 2.8%) but lower than that of RS AHV cells (30/35, 85.7%). Data are

265 means ± s.e.m.; ***$P < 0.001$, ANOVA test (**i**); binomial test (**j**).

No detectable putative monosynaptic connections involving FS HD cells

268 Lastly, given the apparent layer-specific distribution of HD and AHV cells in a cell-type

269 dependent manner, we sought to identify putative monosynaptic connections (Bartho

270 et al., 2004; Csicsvari et al., 1998; Latuske et al., 2015) for a better understanding of

271 functional links between HD, AHV and other cells in the S1HL. We found a small

272 number of RS HD cells made local excitatory (and sometimes reciprocal) connections

273 to both simultaneously recorded RS and FS cells (27/458 pairs; 5.9%; **Fig. 6a**).

274 Surprisingly, there were no identified putative monosynaptic connections between FS

275 HD cells from 251 simultaneously recorded cell pairs. The spike-time cross-

276 correlogram of two simultaneously recorded FS HD cells on the same tetrode showed

277 no detectable synaptic connection (e. g. **Supplementary Fig. S8**). Comparable to RS

278 HD cells, 5.8% of simultaneously recorded cell pairs (19/323) involving RS AHV cells

279 made excitatory connections with both RS and FS cells – mainly with other AHV cells

280 (**Fig. 6b**). A large proportion of cell pairs (7.7%; 41/532) involving FS AHV cells were

281 found to make inhibitory connections to RS and FS, including that are tuned to AHV

282 themselves (**Fig. 6c**). We were also able to detect putative common input-driven of FS
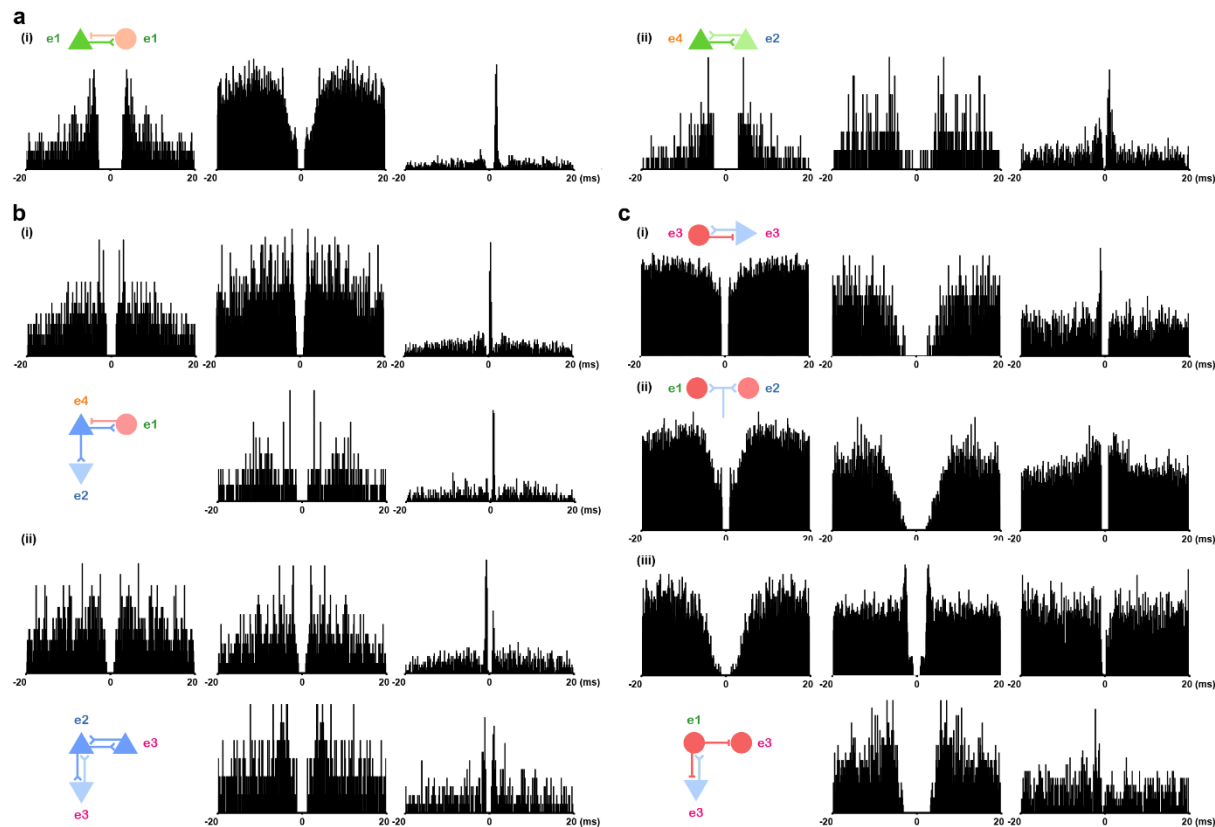
283 AHV cells (**Fig. 6c-ii**).

Fig.6: Putative monosynaptic connections between HD/AHV cells and simultaneously recorded neurons.

a, Two representative monosynaptic connections as revealed by the spike-time cross-correlogram. Left, autocorrelogram of the reference cell; Middle, autocorrelogram of the target cell; Right, cross-correlogram. Hypothesized synaptic connectivity is indicated at the top left of each pair. The tetrode number (e1-e4) is labeled on the left corner of each representative cell. **b**, Putative monosynaptic connections between regular-spiking AHV cells and simultaneously recorded neurons. **c**, Putative monosynaptic connections between fast-spiking AHV cells and simultaneously recorded neurons.

Discussion

Our previous report showed all currently recognized spatial cell types can be found in the S1HL, including HD cells (Long and Zhang, 2018). In this study, we include AHV as an additional spatial feature the S1HL cells also encode. In contrast to a predominant excitatory cell exhibiting HD tuning described elsewhere in the brain, we show disproportionate large numbers of putative interneurons code HD with higher precision than their putative excitatory neuron counterparts. Together, we present a

302 novel configuration of HD circuitry in the S1HL that is dissimilar to those described
303 previously in canonical HD systems.

Fast-spiking cells are tuned to head direction in S1HL

305 While spatially related firing activities have been thought to be mostly confined to the
306 hippocampal-entorhinal system (Moser et al., 2017), the existence of HD cells outside
307 the canonical HD/spatial circuits is not new. Head direction selectivity has been
308 reported in the lateral dorsal thalamic nucleus (Mizumori and Williams, 1993), the
309 striatum (Mehlman et al., 2019; Mizumori et al., 2000; Ragozzino et al., 2001; Wiener,
310 1993), motor cortex (Mehlman et al., 2019; Mizumori et al., 2005), visual cortex (Chen
311 et al., 1994) and the nucleus reuniens (Jankowski et al., 2014). Sharply tuned HD cells
312 have been reported in the layer 2/3 of the MEC. These cells were not classified as FS
313 or putative interneurons (Zutshi et al., 2018). The only reported putative interneuron
314 tuning of HD is in the hippocampus, where HD cells appear to be exclusively FS cells
315 (Leutgeb et al., 2000). Thus, our discovery of sharply tuned FS HD cells co-existing
316 with less well-tuned RS HD cells represents a novel and unique observation specific
317 to the S1HL.

Fast-spiking cells are better tuned than regular-spiking cells to head direction

320 The most surprising finding in our study is that 10% of all recorded FS are HD cells,
321 whereas only ~5% of RS and unclassified cells are HD. In fact, if we restrict HD
322 classification to include only non-conjunctive HD cells, FS HD cell proportionally
323 outnumbers RS or unclassified HD cells 5:1 (10% vs 2%). Our data indicate RS HD
324 cells are similar to those described elsewhere (Preston-Ferrer et al., 2016; Tsanov et
325 al., 2011; Tukker et al., 2015), demonstrating: 1) firing characteristics of putative
326 excitatory principal cells and; 2) are mostly theta-modulated. In past studies examining
327 HD representation in the canonical HD circuit, FS cells were either excluded for spatial
328 selectivity analysis (Coletta et al., 2018) or have been shown to weakly tuned to HD
329 (Peyrache et al., 2019; Tukker et al., 2015) but better tuned to AHV (Preston-Ferrer et
330 al., 2016). These past studies are consistent with previous work elsewhere in sensory
331 and spatial systems, showing that FS cells are poorly tuned to manipulated input
332 features (Atallah et al., 2012; Cardin et al., 2007; Grieves and Jeffery, 2017; Kato et
333 al., 2013; Kerlin et al., 2010; Miyamichi et al., 2013; Zariwala et al., 2011) but may be

334   better suited for coding speed (Gois and Tort, 2018; Kropff et al., 2015; Preston-Ferrer
335   et al., 2016; Ye et al., 2018). However, in the cat visual cortex (Cardin et al., 2007;
336   Runyan et al., 2010), mouse auditory cortex (Moore and Wehr, 2013), as well as in
337   the motor cortex of monkeys (Merchant et al., 2008), FS/putative PV interneurons can
338   exhibit stimulus selectivity comparable to principal cells. Particularly, Cardin and
339   colleagues found all FS cells in layer 4, but not other layers, are sharply tuned to the
340   spatial orientation of presented visual stimuli and are only marginally broader than RS
341   cell tuning (Cardin et al., 2007). Given HD tuning across the whole population at any
342   given HD is coherent (Peyrache et al., 2015), unlike in other systems where input
343   selectivity is heterogeneous and overlapping (Isaacson and Scanziani, 2011), having
344   divergent but homogeneous HD input may drive sharp FS HD tuning in the S1HL.
345   However, our current data suggest FS HD cells are not locally connected, which
346   indicates these FS cells may not be conventional PV+ neurons that have extensive
347   local connections (Koelbl et al., 2015). High-density silicone probe recordings (Bartho
348   et al., 2004; Csicsvari et al., 1998) and cell-type-specific tracing studies (Weible et al.,
349   2010) may provide further insight on the identities and connectivity of FS HD cells
350   reported here. To the best of our knowledge, no previous study has shown FS cells or
351   putative PV+ interneurons displaying superior stimulus selectivity than their
352   RS/putative excitatory cell counterparts. While the neurochemical identity of our FS
353   HD cells remains to be elucidated, we provide the first *prima facie* evidence that
354   putative PV+ interneurons can have sharply tuned feature selectivity.

Generation of HD and AHV activity in the S1HL

356   The presence of AHV cells in the S1HL opens up the possibility that HD selectivity can
357   be locally generated in S1HL. We show both symmetrical and asymmetrical AHV cells
358   are more likely to be putative inhibitory interneurons (i.e. FS cells). Along with RS/
359   putative excitatory HD cells, all basic components of a theorized ring attractor are
360   available within the S1HL for *de novo* HD signal generation (Stratton et al., 2010).
361   However, none of the brain areas exhibiting HD tuning examine so far is independent
362   of the canonical HD circuit (Bassett et al., 2007; Blair et al., 1998; Clark and Taube,
363   2012; Goodridge and Taube, 1997; Mehlman et al., 2019); our S1HL HD cells are
364   unlikely to be different. In our previous report, we suggested that S1HL spatial
365   selectivity is likely to be an efferent copy inherited from elsewhere, possibly from motor
366   areas given their extensive functional and anatomical connections (Long and Zhang,

367 2018). HD and AHV signals from the motor cortex (Mehlman et al., 2019; Mizumori et

368 al., 2005; Wiener, 1993) may arrive through projections to layer 5 (Veinante and

369 Deschenes, 2003), consistent with our observation of FS HD cell enrichment at the

370 border of layer 4/5. Layer 4 is a focal point for thalamocortical input via the ventral

371 posterolateral nucleus (VPL). PV expression can be detected at highest levels across

372 layers 4 and 5 in mice (Almasi et al., 2019; Meyer et al., 2011; Narayanan et al., 2017)

373 and appear to be selectively enriched in layer 4 in rats (Bodor et al., 2005), where

374 thalamic inputs strongly target and activate PV+ neurons (Cruikshank et al., 2007;

375 Sermet et al., 2019) in the vibrissae S1. Thalamic afferents, particularly from VPL

376 where vestibular inputs have been reported (Nagata, 1986), may constitute a novel

377 alternative pathway for establishing HD signalling in the S1HL.

Functional significance of sharply tuned FS HD cells in the S1HL

379 In the S1HL, the general rule of FS are only weakly or broadly tuned to sensory input

380 holds true for tactile stimuli (Hayashi et al., 2018; Murray and Keller, 2011), but our

381 data suggest HD representation is sharply tuned. What is the functional significance

382 of having putative inhibitory interneurons sharply tuned to HD? Firstly, it is entirely

383 possible that these sharply tuned putative interneurons carry out the same proposed

384 function elsewhere in the brain – to further refine principal cell HD representation.

385 Although we have shown that RS HD representation is largely less well-tuned than FS

386 cells, it is entirely possible that RS HD representation may be weaker without FS HD

387 refinement. Optogenetic modulation of layer 4/5 PV+ neurons in restrained animals

388 will be required to provide supporting evidence for sharply tuned FS HD cells to

389 participate in improved HD tuning in principal cells. Gain control is another proposed

390 function for inhibition in the cortex. Bidirectional optogenetic modulation of PV+

391 neurons imposed gain control in visual and auditory systems instead of drastically

392 changing principal cell tuning (Atallah et al., 2012; Moore and Wehr, 2013; Wilson et

393 al., 2012). Sharp tuning of putative inhibitory cells described here may relate to the

394 need to decrease the gain of HD signal within the S1HL, which is compatible with the

395 supposition that spatial representation in the S1 may relate to body parts in space,

396 rather than the whole organism (Brecht, 2017; Long and Zhang, 2018). Alternatively,

397 it has been shown in the vibrissae S1, thalamic-mediated feedforward inhibition is key

398 to suppress motor contributions to somatosensation (Yu et al., 2016). In this scheme,

399 we assume motor inputs at least partially drive spatial responses in the S1HL; sharply

400 tuned FS HD cells may provide the strong inhibition to delineate current HD (sensory)
401 from future (motor) HD.

402 In this study, we carried out the first in-depth characterization of spatial representation
403 in the S1HL (Long and Zhang, 2018). We show a relatively high proportion of putative
404 inhibitory FS cells code for HD with better precision than their RS, putative principal
405 cell counterparts. These data challenge the prevailing view of cortical FS cell function
406 in general, and how HD information is utilized in the brain. The unequivocal anatomical
407 classification of reported FS HD cells is crucial for unlocking an apparent novel cortical
408 mode of operation and (spatial) feature selection.

Materials and Methods

Subjects

411 Seven male Long-Evans rats (2-4 months old, 250-450 grams at the time of the
412 surgery) were used for this study. All animals were housed in groups of four prior to
413 surgery and singly housed in transparent cages (35 cm x 45 cm x 45 cm, W x L x H)
414 and maintained on a 12-hour reversed light-dark cycle (lights on at 9 p.m. and off at 9
415 a.m.) after surgery. Experiments were performed during the dark phase. Rats were
416 maintained in a vivarium with controlled temperature (19-22°C), humidity (55-65%).
417 and were kept at about 85-90% of free-feeding body weight. Food restriction was
418 imposed 8-24 hours before each training and recording trial. Water was available *ad*
419 *libitum*. All animal experiments were performed in accordance with the National Animal
420 Welfare Act under a protocol approved by the Animal Care and Use Committees from
421 both Army Medical University and Xinqiao Hospital.

Surgery and tetrode placement

423 Rats were anesthetized with isoflurane for implant surgery. The local anaesthetic
424 lidocaine was applied to the scalp before the incision was made. Microdrives loaded
425 with four tetrodes were implanted to target the hindlimb region of the primary
426 somatosensory cortex (anterior-posterior (AP): 0.2-2.2 mm posterior to bregma;
427 medial-lateral (ML): 2.2-3.4 mm lateral to midline, dorsal-ventral (DV): 0.4/0.6-3 mm
428 below the dura.), secured with dental cement with 8-10 anchor screws. One screw
429 served as the ground electrode. Rats were given Temgesic as post-op analgesic.

430 Tetrodes were assembled with four 17 μm Platinum/Iridium wires (#100167, California
431 Fine Wire Company). Tetrodes had impedances between 150 and 300 kΩ at 1 kHz
432 through electroplating (nanoZ; White Matter LLC).

Training and data collection

434 Behavioral training, tetrode advancement, and data recording started a week after
435 surgery. Rats were trained to forage in a 1 m x 1 m square box with a white cue card
436 (297 mm x 210 mm) mounted on one side of the wall. Food pellets were scattered into
437 the arena intermittently to encourage exploration.

438 Each recording session lasted between 20 and 40 min to facilitate full coverage of the
439 testing arena. Tetrodes were advanced in steps of 25 or 50 μm daily until well-
440 separated single units can be identified. Data were acquired by an Axona system
441 (Axona Ltd., St. Albans, U.K.) at 48 kHz, band-passed between .8-6.7 kHz and a gain
442 of x 5-18k. Spikes were digitized with 50 8-bit sample windows. Local field potentials
443 were recorded from one of the electrodes with a low-pass filter (500 Hz).

Spike sorting, cell classification and rate map

445 Spike sorting was manually performed offline with TINT (Axona Ltd, St. Albans, U.K.),
446 and the clustering was primarily based on features of the spike waveform (peak-to-
447 trough amplitude and spike width), together with additional autocorrelations and cross-
448 correlations (Skaggs et al., 1996; Wilson and McNaughton, 1993). During our manual
449 cluster cutting, we always counted neurons with similar or identical waveform shapes
450 only once across consecutive recording sessions. Putative fast-spiking interneurons
451 were classified as cells with an average firing rate above 3 Hz and a peak-to-trough
452 spike width below 300 μs (Peyrache et al., 2012).

453 Two small light-emitting diodes (LEDs) were mounted to the headstage to track the
454 rats' position and orientation via an overhead video camera. Only spikes with
455 instantaneous running speeds > 2.5 cm/s were chosen for further analysis in order to
456 exclude confounding behaviors such as immobility, grooming, and rearing (Zhang et
457 al., 2013).

458 To classify firing fields and firing rate distributions, the position data were divided into
459 2.5-cm x 2.5-cm bins, and the path was smoothed with a 21-sample boxcar window

460 filter (400 ms; 10 samples on each side) (Boccara et al., 2010; Zhang et al., 2013).

461 Cells with > 100 spikes per session and with a coverage of >80% were included for

462 further analyses. Maps for spike numbers and spike times were smoothed with a

463 quasi-Gaussian kernel over the neighboring 5 x 5 bins (Zhang et al., 2013). Spatial

464 firing rates were calculated by dividing the smoothed map of spike numbers with spike

465 times. The peak firing rate was defined as the highest rate in the corresponding bin in

466 the spatial firing rate map. Mean firing rates were calculated from the whole session

467 data. Spatial autocorrelation was calculated with smoothed rate maps (Boccara et al.,

468 2010; Zhang et al., 2013). Autocorrelograms were derived from Pearson's product-

469 moment correlation coefficient correcting for edge effects and unvisited locations.

Analysis of head direction cells

471 The rats' head direction was estimated by the relative position of the LEDs

472 differentiated through their sizes (Taube, 1995; Zhang et al., 2013). The directional

473 tuning curve for each recorded cell was drawn by plotting the firing rate as a function

474 of the rat's head angle, which is divided into bins of 3 degrees and then smoothed with

475 a 14.5-degree mean window filter (2 bins on each side). To avoid bias, data were only

476 used if all head angle bins contain data (Zhang et al., 2013).

477 The strength of directionality was calculated by computing the mean vector length from

478 circular distributed firing rates. The chance values were determined by a shuffling

479 process, with the entire sequence of spike trains time-shifted between 20 s and the

480 whole trail length minus 20 s along the animals' trajectory. This shuffling process was

481 repeated 100 times for each cell, generating a total of 210,700 permutations for the

482 2107 somatosensory neurons. This shuffling procedure preserved the temporal firing

483 characteristics in the unshuffled data while disrupting the spatial structure at the same

484 time. Cells were defined as head direction cells if the mean vector lengths of the

485 recorded cells were larger than the 99th percentile of the mean vector lengths in the

486 shuffled distribution.

Analysis of angular head velocity cells

488 The modulation of firing rate by animals' angular head velocity (AHV) was calculated

489 as previously described (Taube, 1995). Briefly, the first derivative of head direction

490 (angular velocity) for each time sample was computed. For each cell, the firing rate

491 was plotted as a function of AHV in 6 degree/s bin. To minimize the sampling bias,
492 bins with less than 50 samples per second were excluded. The AHV score was defined
493 by calculating the Pearson's correlation coefficient between the angular head velocity
494 and firing rate. Shuffling was performed in the same procedure used for defining head
495 direction cells. Cells were defined as AHV cells if the AHV scores of the recorded cells
496 were larger than 0.5.

Analysis of theta modulation and power spectral density

498 To calculate fluctuations of neural activity through the theta cycle, we offline-filtered
499 local field potentials (LFPs) to extract S1HL theta oscillations. For the low-pass filtering,
500 4 and 5 Hz were selected as stopband and passband low cut-off frequencies,
501 respectively, while 10 and 11 Hz were selected as passband and stopband high cut-
502 off frequencies, respectively. Theta modulation was calculated from the fast Fourier
503 transform (FFT)-based power spectrum of the spike-train autocorrelation. When the
504 mean spectral power within 1 Hz range of the theta peak within the 4-11 Hz frequency
505 range was at least 5 times larger than the mean spectral power from 0 Hz to 125 Hz,
506 the cell was classified as theta modulated. To quantify the theta rhythmicity of the local
507 field potentials (LFP) within the somatosensory cortex, the LFP was bandpass-filtered
508 with the theta range (4-11 Hz) to acquire theta-filtered LFP traces. Power spectral
509 density was computed with FFT.

Analysis of Bursty Firing Properties

511 We analyzed the interspike interval (ISI) histogram to determine the bursty discharge
512 patterns as described previously (Ebbesen et al., 2016). ISI probability distribution was
513 first computed for each head direction cell by binning the ISIs below 60 ms with 1 ms
514 bins and normalized that the area under the curve equals 1. Then a principal
515 component analysis (MATLAB, MathWorks) was performed on the ISI probability
516 distributions for all the neurons and the first two principal components (PC1 and PC2)
517 were obtained, followed by a 2D Gaussian kernel smoothed density estimate (Botev
518 et al., 2010).

Cross-correlogram and putative synaptic connections

520 We identified putative monosynaptic connections by using spike-time cross-
521 correlograms as described by others (Bartho et al., 2004; Csicsvari et al., 1998). Briefly,

522   short-latency (< 4ms) peaks with the amplitude above 5 SDs of baseline mean of the

523   cross-correlograms were considered as putative monosynaptic excitatory connections.

524   Similarly, short-latency (< 4ms) troughs with the amplitude below 5 SDs of baseline

525   mean of the cross-correlograms were considered as putative monosynaptic inhibitory

526   connections. For simultaneously recorded neuron pairs on the same tetrode, the 0-1

527   ms bins of the cross-correlogram were not considered due to the unresolved

528   superimposed spikes.

Histology and reconstruction of recording positions

530   At the end of the experiment, rats were euthanized with an overdose of sodium

531   pentobarbital and perfused transcardially with phosphate-buffered saline (PBS)

532   followed by 4% paraformaldehyde (PFA). Brains were removed and stored in 4% PFA

533   overnight. The brain was then placed in 10, 20 and 30% sucrose/PFA solution

534   sequentially across 72 hours before sectioning using a cyrotome. Thirty-micron

535   sections were obtained through the implant region. Sections were mounted on glass

536   slides and stained with cresyl violet (Sigma-Aldrich). The final recording positions were

537   determined from digitized images of the Nissl-stained sections. Positions of each

538   recording were estimated from the deepest tetrode track, notes on tetrode

539   advancement with tissue shrinkage correction by dividing the distance between the

540   brain surface and electrode tips by the last advanced depth of the recording electrodes.

541   All electrode traces were confirmed to be located within the S1defined by The Rat

542   Brain Atlas (Paxinos and Watson, 2007).

550   **Author Contributions:** S.-J.Z. conceived the project. X.L., C.K.Y. and S.-J.Z.

551   designed the study. X.L. and S.-J.Z. performed the experiments and collected the data.

552   X.L. and C.K.Y. analyzed the data and made the figures. X.L., C.K.Y. and S.-J.Z. wrote

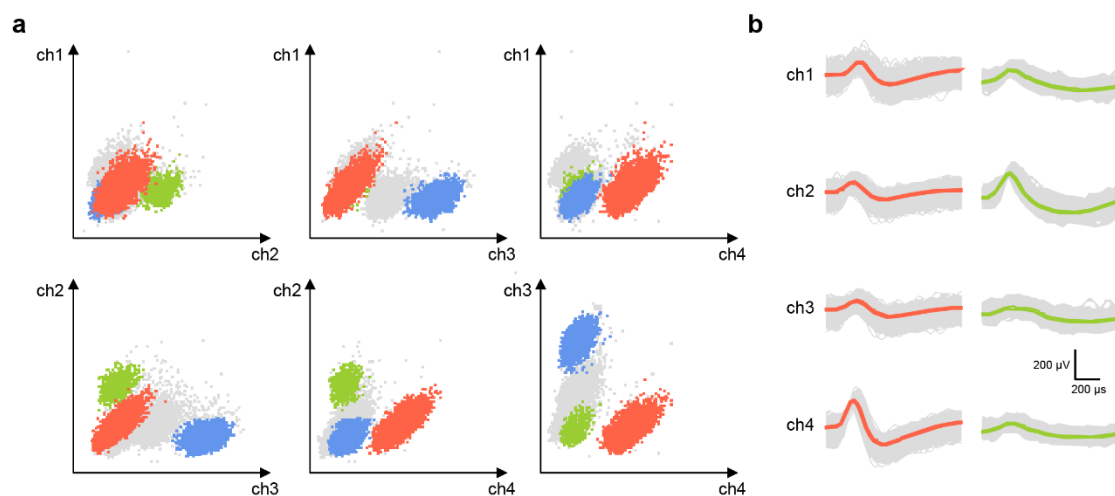553   the manuscript.

554 **Competing interests**

555 The authors declare no competing interests.

556 **Supplementary Information**

557 This file contains Supplementary figures S1-S8.

558 **Data and Code Availability**

559 The data and source code that support the findings of this study are available from

560 the corresponding author upon reasonable request.

561

562 **Supplementary Fig. S1: Cluster diagrams and waveforms recorded from the**

563 **hindlimb region of the primary somatosensory cortex.**

564 (**a**) Scatterplots show the relationship between peak-to-trough amplitudes for all spikes,

565 which are recorded on six types of permutation and combination from all of four

566 tethered electrodes (ch1-ch4) on a specific tetrode. Each dot represents a single

567 recorded spike. (**b**) Waveforms from two separated FS (red) and RS (green) clusters

568 in the scatterplots are shown from four electrodes on the same recorded tetrode based

569 on the shape of waveforms and the average firing rates. The cluster diagrams show

570 spike clusters are well separated from our recordings in the S1HL.

571
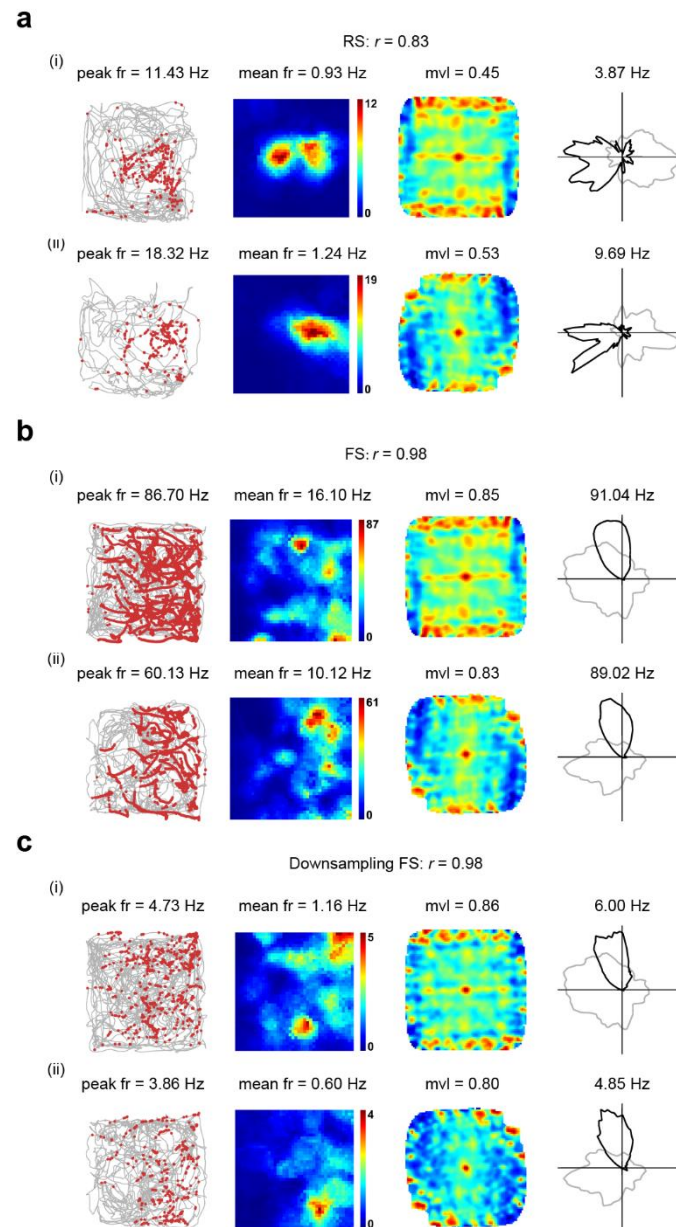
**Supplementary Fig. S2: Angular stability of S1HL head direction cells.**

a-c, Intra-trial angular stability between the first and second halves of RS, FS and downsampled FS HD cells from **Fig. 2a**. From left to right: trajectory (grey line) with superimposed spike locations (red dots); smoothed rate maps; spatial autocorrelation; and HD tuning curve (black) plotted against dwell-time (grey) for the first half (**i**) and the second half (**ii**) of the trials. Firing rate is color-coded with blue indicating minimum firing rate and red indicating maximum firing rate. The scale of the autocorrelation maps is twice that of the spatial firing rate maps. Peak firing rate (fr), mean fr, mean vector length (mvl) and angular peak rate for each representative HD cell are labeled at the top of the panels. Correlation coefficients of the distributed firing rate across all

582 directional bins between the first and second halves of individual recording trials are

583 indicated with *r*.

584
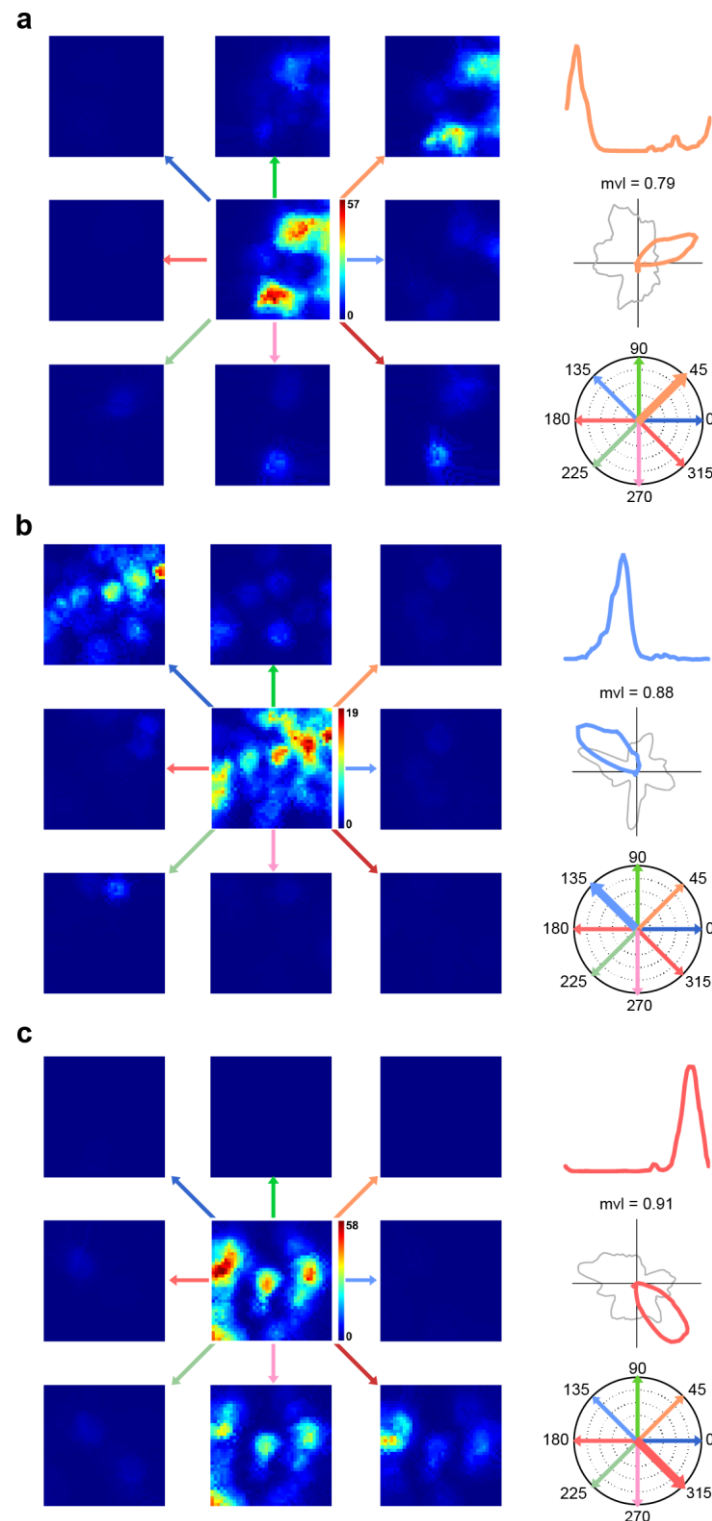
Supplementary Fig. S3: No positional bias in head direction tuning in S1HL FS head direction cells

587   **a-c**, Three examples of S1HL FS HD cells recorded from freely moving rats. For each
588   recorded FS HD cell, 8 smoothed rate maps across all eight HD sectors are shown in
589   the following plots. Left, one spatial firing rate map of a single FS HD cell is divided
590   into eight smoothed rate maps across all eight HD sectors segmented by 45° each.
591   Top right, HD tuning curve. Middle right, firing rate polar plots plotted against dwell-
592   time polar plot (grey). Bottom right, circular distribution of the preferred firing direction
593   across 360°.

594
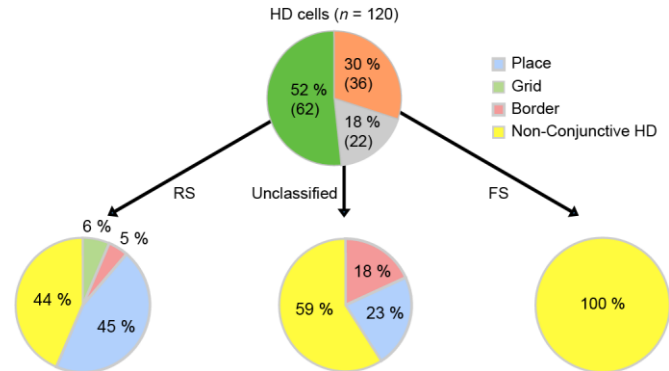
595   **Supplementary Fig. S4: Classification of somatosensory head direction cells.**

596   Pie diagram showing the classification of fast-spiking (FS), regular-spiking (RS) and
597   unclassified head direction (HD) cells into conjunctive and non-conjunctive HD cells.

598
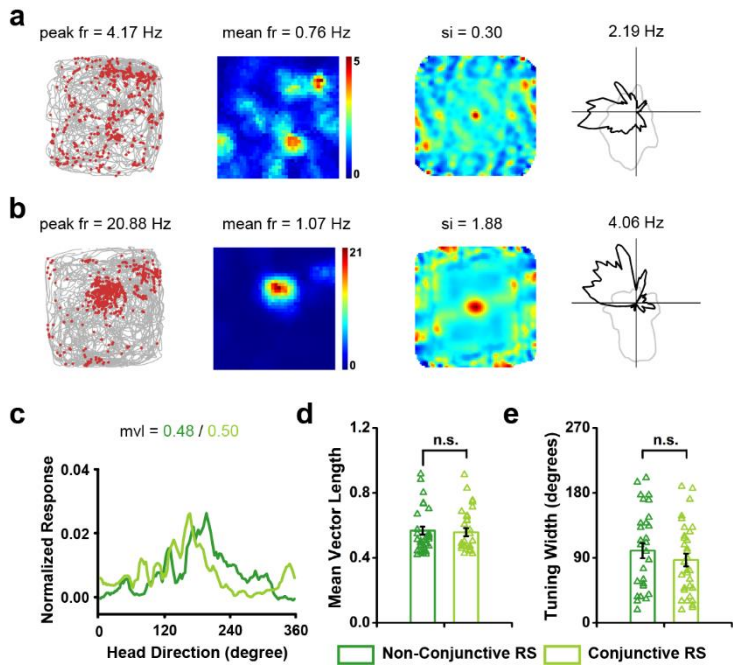
599   **Supplementary Fig. S5: Conjunctive and non-conjunctive regular-spiking cells**
600   **show similar head directional tuning.**

601 **a**, Representative non-conjunctive RS HD and **b,** conjunctive RS HD x place cells.

602 From left to right: trajectory (grey line) with superimposed spike locations (red dots);

603 smoothed rate maps; spatial autocorrelation; and HD tuning curve (black) against

604 dwell-time (grey). **c**, Normalized head direction tuning curve for the non-conjunctive

605 (dark green) and conjunctive (light green) RS HD cells. **d**, Non-conjunctive RS HD

606 cells (dark green, *n* = 30) and conjunctive RS HD cells (dark green, *n* = 30) have an

607 indistinguishable mean vector length. **e**, Non-conjunctive RS HD cells show

608 comparable tuning width as conjunctive RS HD cells.

609
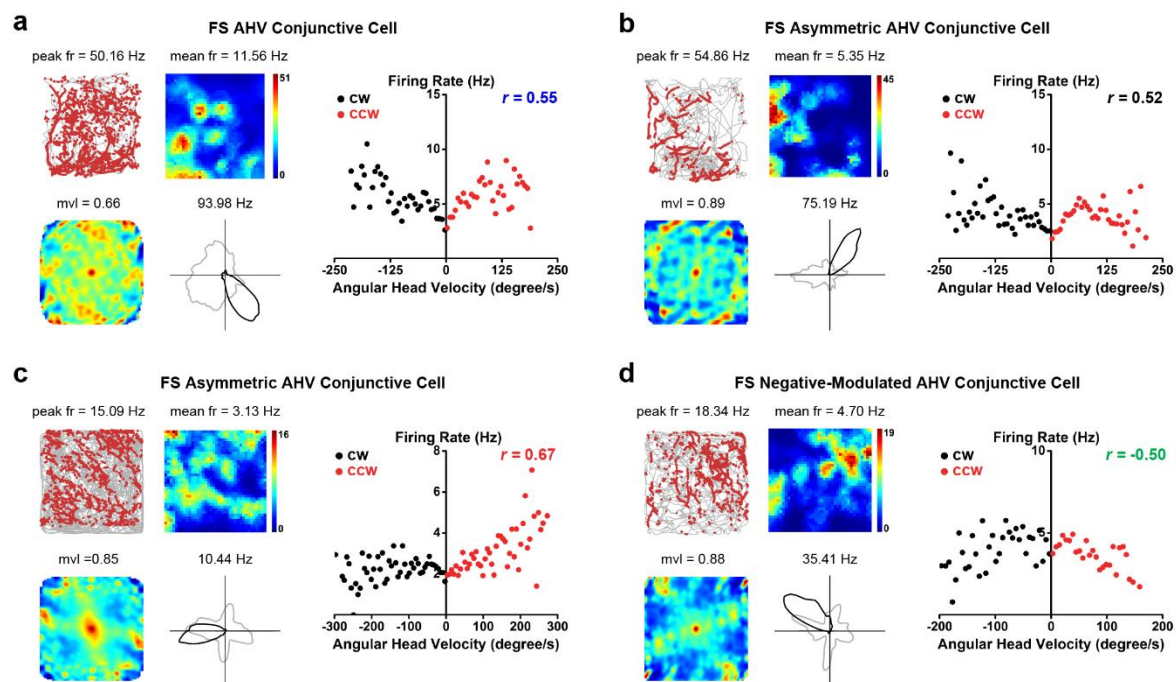
610 **Supplementary Fig. S6: Conjunctive FS HD × AHV cells.**

611 **a-d**, Four representatives of conjunctive FS HD × AHV cells. **a**, FS HD cell with positive

612 AHV modulation; **b**, FS HD cell with asymmetrical (CW) AHV modulation; **c**, FS HD

613 cell with asymmetrical (CCW) AHV modulation; **d**, FS HD cell with symmetrical

614 negative AHV modulation. Left panel: Trajectory (grey line) with superimposed spike

615 locations (red dots; top left), smoothed rate maps (top right), spatial autocorrelation

616 (bottom left) and HD tuning curve (black) plotted against dwell-time (grey; bottom right).

617 Firing rate is color-coded with dark blue indicating minimal firing rate and dark red

618 indicating maximal firing rate. The scale of the autocorrelation maps is twice that of

619 the spatial firing rate maps. Peak firing rate (fr), mean fr, mean vector length (mvl) and

620 angular peak rate for each representative head direction cell are labelled at the top of

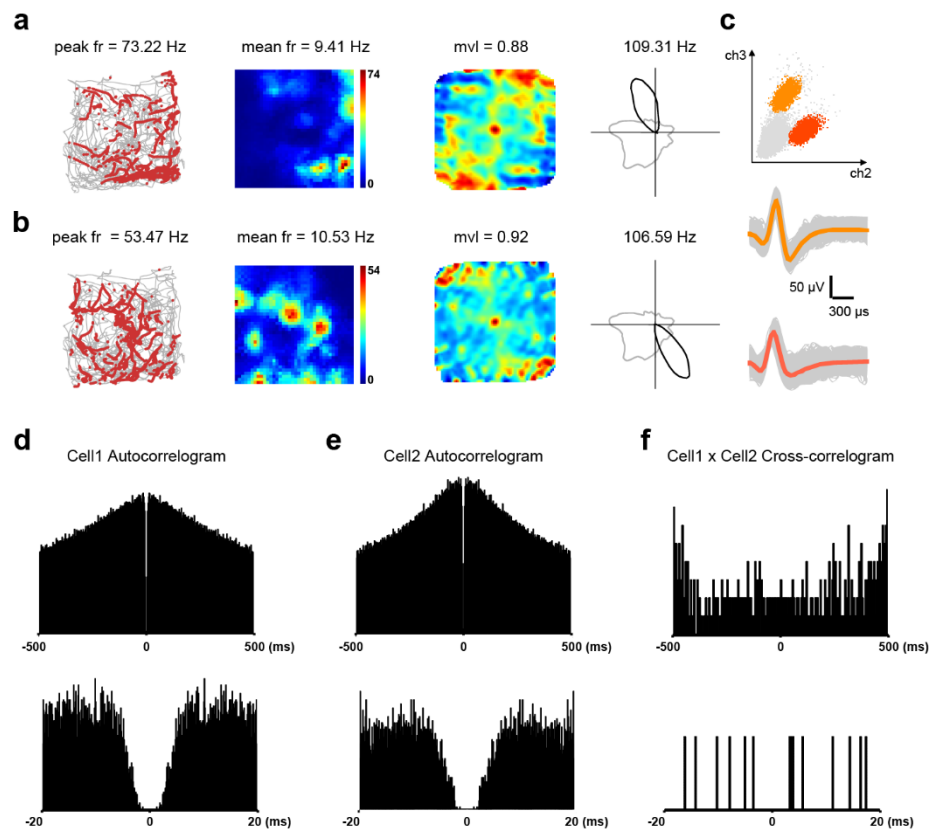621   the panels. Right panel: Scatterplot of the firing rate versus the angular velocity of the

622   representative cells.

623
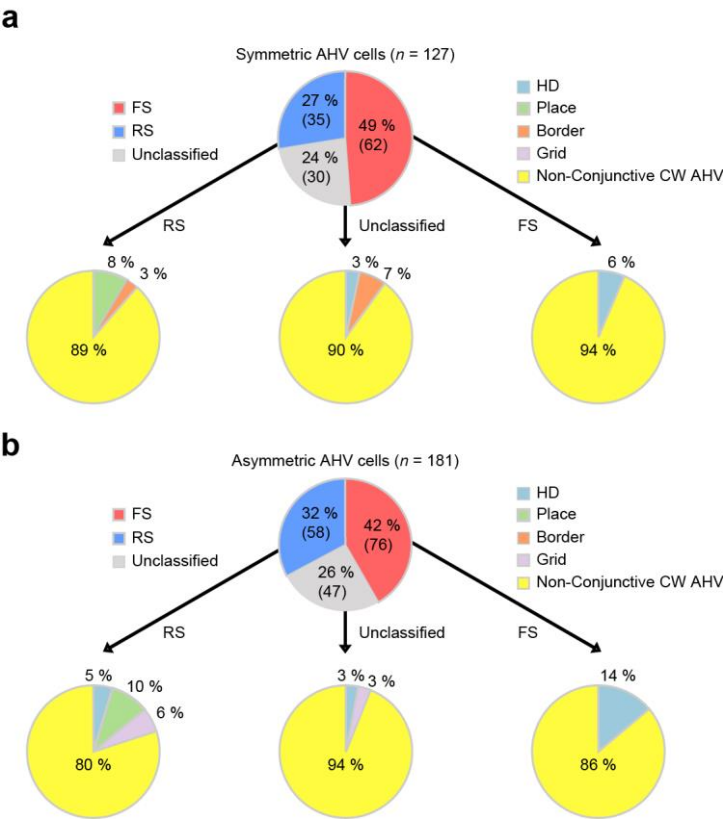
Supplementary Fig. S7: Classification of S1HL AHV cells.

625   **a**, Pie diagram showing the composition of three neuronal types of symmetric AHV

626   cells. **b**, Pie diagram showing the composition of three neuronal types of asymmetric

627   AHV cells.

Supplementary Fig. S8: Two simultaneously recorded FS HD cells on the same tetrode.

a, **b**, Two simultaneously recorded FS somatosensory HD cells from the same tetrode. Trajectory (grey line) with superimposed spike locations (red dots) (left column); spatial firing rate maps (middle left column), autocorrelation diagrams (middle right column), head direction tuning curves (black) plotted against dwell-time polar plot (grey) (right column). **c**, Cluster diagrams and waveforms. **d**, **e**, Representative 1000 ms spike-time autocorrelogram plot of the two representative somatosensory FS HD cells. **f**, Representative 1000 ms spike-time cross-correlogram of two exampled cells above. Bottom panels of **d-f**, shorter time scale of autocorrelogram and cross-correlogram.

References

Almasi, Z., David, C., Witte, M., and Staiger, J.F. (2019). Distribution Patterns of Three Molecularly Defined Classes of GABAergic Neurons Across Columnar Compartments in Mouse Barrel Cortex. Front Neuroanat *13*, 45.

644   Atallah, B.V., Bruns, W., Carandini, M., and Scanziani, M. (2012). Parvalbumin-expressing
645   interneurons linearly transform cortical responses to visual stimuli. Neuron *73*, 159-170.
646   Bartho, P., Hirase, H., Monconduit, L., Zugaro, M., Harris, K.D., and Buzsaki, G. (2004).
647   Characterization of neocortical principal cells and interneurons by network interactions and
648   extracellular features. J Neurophysiol *92*, 600-608.
649   Bassett, J.P., Tullman, M.L., and Taube, J.S. (2007). Lesions of the tegmentomammillary circuit in the
650   head direction system disrupt the head direction signal in the anterior thalamus. J Neurosci *27*,
651   7564-7577.
652   Blair, H.T., Cho, J., and Sharp, P.E. (1998). Role of the lateral mammillary nucleus in the rat head
653   direction circuit: a combined single unit recording and lesion study. Neuron *21*, 1387-1397.
654   Blair, H.T., Cho, J., and Sharp, P.E. (1999). The anterior thalamic head-direction signal is abolished by
655   bilateral but not unilateral lesions of the lateral mammillary nucleus. The Journal of neuroscience :
656   the official journal of the Society for Neuroscience *19*, 6673-6683.
657   Boccara, C.N., Sargolini, F., Thoresen, V.H., Solstad, T., Witter, M.P., Moser, E.I., and Moser, M.B.
658   (2010). Grid cells in pre- and parasubiculum. Nat Neurosci *13*, 987-994.
659   Bodor, A.L., Katona, I., Nyiri, G., Mackie, K., Ledent, C., Hajos, N., and Freund, T.F. (2005).
660   Endocannabinoid signaling in rat somatosensory cortex: laminar differences and involvement of
661   specific interneuron types. J Neurosci *25*, 6845-6856.
662   Bolding, K.A., Ferbinteanu, J., Fox, S.E., and Muller, R.U. (2019). Place cell firing cannot support
663   navigation without intact septal circuits. Hippocampus.
664   Botev, Z.I., Grotowski, J.F., and Kroese, D.P. (2010). Kernel Density Estimation Via Diffusion. Ann Stat
665   *38*, 2916-2957.
666   Brandon, M.P., Bogaard, A.R., Libby, C.P., Connerney, M.A., Gupta, K., and Hasselmo, M.E. (2011).
667   Reduction of theta rhythm dissociates grid cell spatial periodicity from directional tuning. Science
668   *332*, 595-599.
669   Brecht, M. (2017). The Body Model Theory of Somatosensory Cortex. Neuron *94*, 985-992.
670   Burgess, N., and O'Keefe, J. (2011). Models of place and grid cell firing and theta rhythmicity. Curr
671   Opin Neurobiol *21*, 734-744.
672   Calton, J.L., Stackman, R.W., Goodridge, J.P., Archey, W.B., Dudchenko, P.A., and Taube, J.S. (2003).
673   Hippocampal place cell instability after lesions of the head direction cell network. J Neurosci *23*,
674   9719-9731.
675   Cardin, J.A., Palmer, L.A., and Contreras, D. (2007). Stimulus feature selectivity in excitatory and
676   inhibitory neurons in primary visual cortex. J Neurosci *27*, 10333-10344.
677   Chen, L.L., Lin, L.H., Green, E.J., Barnes, C.A., and McNaughton, B.L. (1994). Head-direction cells in
678   the rat posterior cortex. I. Anatomical distribution and behavioral modulation. Exp Brain Res *101*, 8-
679   23.
680   Clark, B.J., and Taube, J.S. (2012). Vestibular and attractor network basis of the head direction cell
681   signal in subcortical circuits. Front Neural Circuits *6*, 7.
682   Coletta, S., Zeraati, R., Nasr, K., Preston-Ferrer, P., and Burgalossi, A. (2018). Interspike interval
683   analysis and spikelets in presubicular head-direction cells. J Neurophysiol *120*, 564-575.
684   Cruikshank, S.J., Lewis, T.J., and Connors, B.W. (2007). Synaptic basis for intense thalamocortical
685   activation of feedforward inhibitory cells in neocortex. Nat Neurosci *10*, 462-468.
686   Csicsvari, J., Hirase, H., Czurko, A., and Buzsaki, G. (1998). Reliability and state dependence of
687   pyramidal cell-interneuron synapses in the hippocampus: an ensemble approach in the behaving rat.
688   Neuron *21*, 179-189.
689   Ebbesen, C.L., Reifenstein, E.T., Tang, Q., Burgalossi, A., Ray, S., Schreiber, S., Kempter, R., and
690   Brecht, M. (2016). Cell Type-Specific Differences in Spike Timing and Spike Shape in the Rat
691   Parasubiculum and Superficial Medial Entorhinal Cortex. Cell reports *16*, 1005-1015.
692   Gois, Z., and Tort, A.B.L. (2018). Characterizing Speed Cells in the Rat Hippocampus. Cell reports *25*,
693   1872-1884 e1874.

694 Goodridge, J.P., and Taube, J.S. (1997). Interaction between the postsubiculum and anterior
695 thalamus in the generation of head direction cell activity. J Neurosci *17*, 9315-9330.
696 Grieves, R.M., and Jeffery, K.J. (2017). The representation of space in the brain. Behav Processes *135*,
697 113-131.
698 Hafting, T., Fyhn, M., Molden, S., Moser, M.B., and Moser, E.I. (2005). Microstructure of a spatial
699 map in the entorhinal cortex. Nature *436*, 801-806.
700 Harland, B., Grieves, R.M., Bett, D., Stentiford, R., Wood, E.R., and Dudchenko, P.A. (2017). Lesions of
701 the Head Direction Cell System Increase Hippocampal Place Field Repetition. Curr Biol *27*, 2706-2712
702 e2702.
703 Hayashi, A., Yoshida, T., and Ohki, K. (2018). Cell Type Specific Representation of Vibro-tactile Stimuli
704 in the Mouse Primary Somatosensory Cortex. Front Neural Circuits *12*, 109.
705 Hok, V., Jacob, P.-Y., Bordiga, P., Truchet, B., Poucet, B., and Save, E. (2018). A spatial code in the
706 dorsal lateral geniculate nucleus. bioRxiv, 473520.
707 Isaacson, Jeffry S., and Scanziani, M. (2011). How Inhibition Shapes Cortical Activity. Neuron *72*, 231-
708 243.
709 Jankowski, M.M., Islam, M.N., Wright, N.F., Vann, S.D., Erichsen, J.T., Aggleton, J.P., and O'Mara,
710 S.M. (2014). Nucleus reuniens of the thalamus contains head direction cells. eLife *3*.
711 Jankowski, M.M., and O'Mara, S.M. (2015). Dynamics of place, boundary and object encoding in rat
712 anterior claustrum. Front Behav Neurosci *9*, 250.
713 Kato, H.K., Gillet, S.N., Peters, A.J., Isaacson, J.S., and Komiyama, T. (2013). Parvalbumin-expressing
714 interneurons linearly control olfactory bulb output. Neuron *80*, 1218-1231.
715 Kerlin, A.M., Andermann, M.L., Berezovskii, V.K., and Reid, R.C. (2010). Broadly tuned response
716 properties of diverse inhibitory neuron subtypes in mouse visual cortex. Neuron *67*, 858-871.
717 Knierim, J.J., Kudrimoti, H.S., and McNaughton, B.L. (1998). Interactions Between Idiothetic Cues and
718 External Landmarks in the Control of Place Cells and Head Direction Cells. Journal of
719 Neurophysiology *80*, 425-446.
720 Koelbl, C., Helmstaedter, M., Lubke, J., and Feldmeyer, D. (2015). A barrel-related interneuron in
721 layer 4 of rat somatosensory cortex with a high intrabarrel connectivity. Cereb Cortex *25*, 713-725.
722 Koenig, J., Linder, A.N., Leutgeb, J.K., and Leutgeb, S. (2011). The spatial periodicity of grid cells is not
723 sustained during reduced theta oscillations. Science *332*, 592-595.
724 Kropff, E., Carmichael, J.E., Moser, M.B., and Moser, E.I. (2015). Speed cells in the medial entorhinal
725 cortex. Nature *523*, 419-424.
726 Latuske, P., Toader, O., and Allen, K. (2015). Interspike Intervals Reveal Functionally Distinct Cell
727 Populations in the Medial Entorhinal Cortex. J Neurosci *35*, 10963-10976.
728 Leutgeb, S., Ragozzino, K.E., and Mizumori, S.J. (2000). Convergence of head direction and place
729 information in the CA1 region of hippocampus. Neuroscience *100*, 11-19.
730 Long, X., and Zhang, S.-J. (2018). A novel somatosensory spatial navigation system outside the
731 hippocampal formation. bioRxiv, 473090.
732 Mehlman, M.L., Winter, S.S., Valerio, S., and Taube, J.S. (2019). Functional and anatomical
733 relationships between the medial precentral cortex, dorsal striatum, and head direction cell circuitry.
734 I. Recording studies. J Neurophysiol *121*, 350-370.
735 Merchant, H., Naselaris, T., and Georgopoulos, A.P. (2008). Dynamic sculpting of directional tuning in
736 the primate motor cortex during three-dimensional reaching. J Neurosci *28*, 9164-9172.
737 Meyer, H.S., Schwarz, D., Wimmer, V.C., Schmitt, A.C., Kerr, J.N., Sakmann, B., and Helmstaedter, M.
738 (2011). Inhibitory interneurons in a cortical column form hot zones of inhibition in layers 2 and 5A.
739 Proc Natl Acad Sci U S A *108*, 16807-16812.
740 Miyamichi, K., Shlomai-Fuchs, Y., Shu, M., Weissbourd, B.C., Luo, L., and Mizrahi, A. (2013).
741 Dissecting local circuits: parvalbumin interneurons underlie broad feedback control of olfactory bulb
742 output. Neuron *80*, 1232-1245.

743   Mizumori, S.J., Puryear, C.B., Gill, K.M., and Guazzelli, A. (2005). Head direction codes in
744   hippocampal afferent and efferent systems: what functions do they serve. Head direction cells and
745   the neural mechanisms of spatial orientation, 203-220.
746   Mizumori, S.J., and Williams, J.D. (1993). Directionally selective mnemonic properties of neurons in
747   the lateral dorsal nucleus of the thalamus of rats. J Neurosci *13*, 4015-4028.
748   Mizumori, S.J.Y., Ragozzino, K.E., and Cooper, B.G. (2000). Location and head direction
749   representation in the dorsal striatum of rats. Psychobiology *28*, 441-462.
750   Moore, A.K., and Wehr, M. (2013). Parvalbumin-expressing inhibitory interneurons in auditory
751   cortex are well-tuned for frequency. J Neurosci *33*, 13713-13723.
752   Moser, E.I., Moser, M.B., and McNaughton, B.L. (2017). Spatial representation in the hippocampal
753   formation: a history. Nat Neurosci *20*, 1448-1464.
754   Murray, P.D., and Keller, A. (2011). Somatosensory response properties of excitatory and inhibitory
755   neurons in rat motor cortex. J Neurophysiol *106*, 1355-1362.
756   Nagata, S. (1986). The vestibulothalamic connections in the rat: a morphological analysis using
757   wheat germ agglutinin-horseradish peroxidase. Brain research *376*, 57-70.
758   Narayanan, R.T., Udvary, D., and Oberlaender, M. (2017). Cell Type-Specific Structural Organization
759   of the Six Layers in Rat Barrel Cortex. Front Neuroanat *11*, 91.
760   O'Keefe, J., and Dostrovsky, J. (1971). The hippocampus as a spatial map. Preliminary evidence from
761   unit activity in the freely-moving rat. Brain Res *34*, 171-175.
762   Paxinos, G., and Watson, C. (2007). The rat brain in stereotaxic coordinates, Vol 552 (Amsterdam:
763   Elsevier).
764   Peyrache, A., Dehghani, N., Eskandar, E.N., Madsen, J.R., Anderson, W.S., Donoghue, J.A., Hochberg,
765   L.R., Halgren, E., Cash, S.S., and Destexhe, A. (2012). Spatiotemporal dynamics of neocortical
766   excitation and inhibition during human sleep. Proc Natl Acad Sci U S A *109*, 1731-1736.
767   Peyrache, A., Duszkiewicz, A.J., Viejo, G., and Angeles-Duran, S. (2019). Thalamocortical processing
768   of the head-direction sense. Progress in Neurobiology *183*, 101693.
769   Peyrache, A., Lacroix, M.M., Petersen, P.C., and Buzsaki, G. (2015). Internally organized mechanisms
770   of the head direction sense. Nat Neurosci *18*, 569-575.
771   Preston-Ferrer, P., Coletta, S., Frey, M., and Burgalossi, A. (2016). Anatomical organization of
772   presubicular head-direction circuits. eLife *5*.
773   Ragozzino, K.E., Leutgeb, S., and Mizumori, S.J. (2001). Dorsal striatal head direction and
774   hippocampal place representations during spatial navigation. Exp Brain Res *139*, 372-376.
775   Runyan, C.A., Schummers, J., Van Wart, A., Kuhlman, S.J., Wilson, N.R., Huang, Z.J., and Sur, M.
776   (2010). Response Features of Parvalbumin-Expressing Interneurons Suggest Precise Roles for
777   Subtypes of Inhibition in Visual Cortex. Neuron *67*, 847-857.
778   Sermet, B.S., Truschow, P., Feyerabend, M., Mayrhofer, J.M., Oram, T.B., Yizhar, O., Staiger, J.F., and
779   Petersen, C.C. (2019). Pathway-, layer- and cell-type-specific thalamic input to mouse barrel cortex.
780   eLife *8*.
781   Sharp, P.E. (1996). Multiple spatial/behavioral correlates for cells in the rat postsubiculum: multiple
782   regression analysis and comparison to other hippocampal areas. Cereb Cortex *6*, 238-259.
783   Sharp, P.E., Tinkelman, A., and Cho, J. (2001). Angular velocity and head direction signals recorded
784   from the dorsal tegmental nucleus of gudden in the rat: Implications for path integration in the head
785   direction cell circuit (US: American Psychological Association), pp. 571-588.
786   Shinder, M.E., and Taube, J.S. (2011). Active and passive movement are encoded equally by head
787   direction cells in the anterodorsal thalamus. Journal of Neurophysiology *106*, 788-800.
788   Shinder, M.E., and Taube, J.S. (2014). Self-motion improves head direction cell tuning. Journal of
789   Neurophysiology *111*, 2479-2492.
790   Skaggs, W.E., McNaughton, B.L., Wilson, M.A., and Barnes, C.A. (1996). Theta phase precession in
791   hippocampal neuronal populations and the compression of temporal sequences. Hippocampus *6*,
792   149-172.

Solstad, T., Boccara, C.N., Kropff, E., Moser, M.B., and Moser, E.I. (2008). Representation of geometric borders in the entorhinal cortex. Science *322*, 1865-1868.

Stackman, R.W., Clark, A.S., and Taube, J.S. (2002). Hippocampal spatial representations require vestibular input. Hippocampus *12*, 291-303.

Stackman, R.W., Golob, E.J., Bassett, J.P., and Taube, J.S. (2003). Passive Transport Disrupts Directional Path Integration by Rat Head Direction Cells. Journal of Neurophysiology *90*, 2862-2874.

Stackman, R.W., and Taube, J.S. (1997). Firing Properties of Head Direction Cells in the Rat Anterior Thalamic Nucleus: Dependence on Vestibular Input. The Journal of Neuroscience *17*, 4349.

Stratton, P., Wyeth, G., and Wiles, J. (2010). Calibration of the head direction network: a role for symmetric angular head velocity cells. J Comput Neurosci *28*, 527-538.

Taube, J.S. (1995). Head direction cells recorded in the anterior thalamic nuclei of freely moving rats. The Journal of Neuroscience *15*, 70.

Taube, J.S., Muller, R.U., and Ranck, J.B., Jr. (1990a). Head-direction cells recorded from the postsubiculum in freely moving rats. I. Description and quantitative analysis. J Neurosci *10*, 420-435.

Taube, J.S., Muller, R.U., and Ranck, J.B., Jr. (1990b). Head-direction cells recorded from the postsubiculum in freely moving rats. II. Effects of environmental manipulations. J Neurosci *10*, 436-447.

Tsanov, M., Chah, E., Vann, S.D., Reilly, R.B., Erichsen, J.T., Aggleton, J.P., and O'Mara, S.M. (2011). Theta-modulated head direction cells in the rat anterior thalamus. The Journal of neuroscience : the official journal of the Society for Neuroscience *31*, 9489-9502.

Tukker, J.J., Tang, Q., Burgalossi, A., and Brecht, M. (2015). Head-Directional Tuning and Theta Modulation of Anatomically Identified Neurons in the Presubiculum. J Neurosci *35*, 15391-15395.

Veinante, P., and Deschenes, M. (2003). Single-cell study of motor cortex projections to the barrel field in rats. J Comp Neurol *464*, 98-103.

Weible, A.P., Schwarcz, L., Wickersham, I.R., Deblander, L., Wu, H., Callaway, E.M., Seung, H.S., and Kentros, C.G. (2010). Transgenic Targeting of Recombinant Rabies Virus Reveals Monosynaptic Connectivity of Specific Neurons. J Neurosci *30*, 16509-16513.

Wiener, S.I. (1993). Spatial and behavioral correlates of striatal neurons in rats performing a self-initiated navigation task. J Neurosci *13*, 3802-3817.

Wilson, M.A., and McNaughton, B.L. (1993). Dynamics of the hippocampal ensemble code for space. Science *261*, 1055-1058.

Wilson, N.R., Runyan, C.A., Wang, F.L., and Sur, M. (2012). Division and subtraction by distinct cortical inhibitory networks in vivo. Nature *488*, 343-348.

Winter, S.S., Clark, B.J., and Taube, J.S. (2015). Spatial navigation. Disruption of the head direction cell network impairs the parahippocampal grid cell signal. Science *347*, 870-874.

Ye, J., Witter, M.P., Moser, M.B., and Moser, E.I. (2018). Entorhinal fast-spiking speed cells project to the hippocampus. Proc Natl Acad Sci U S A *115*, E1627-E1636.

Yu, J., Gutnisky, D.A., Hires, S.A., and Svoboda, K. (2016). Layer 4 fast-spiking interneurons filter thalamocortical signals during active somatosensation. Nature neuroscience *19*, 1647-1657.

Zariwala, H.A., Madisen, L., Ahrens, K.F., Bernard, A., Lein, E.S., Jones, A.R., and Zeng, H. (2011). Visual tuning properties of genetically identified layer 2/3 neuronal types in the primary visual cortex of cre-transgenic mice. Front Syst Neurosci *4*, 162.

Zhang, K. (1996). Representation of spatial orientation by the intrinsic dynamics of the head-direction cell ensemble: a theory. J Neurosci *16*, 2112-2126.

Zhang, S.J., Ye, J., Miao, C., Tsao, A., Cerniauskas, I., Ledergerber, D., Moser, M.B., and Moser, E.I. (2013). Optogenetic dissection of entorhinal-hippocampal functional connectivity. Science *340*, 1232627.

Zutshi, I., Fu, M.L., Lilascharoen, V., Leutgeb, J.K., Lim, B.K., and Leutgeb, S. (2018). Recurrent circuits within medial entorhinal cortex superficial layers support grid cell firing. Nature Communications *9*, 3701.